Soils and Foundations 2014;54(4):731–747

The Japanese Geotechnical Society

Soils and Foundations

www.sciencedirect.com
journal homepage: www.elsevier.com/locate/sandf

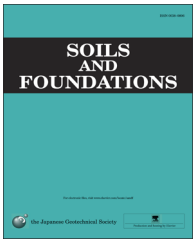

Change in the hydromechanical characteristics of embankment material due to compaction state conditions

Shoji Yokohama[a,*], Seiichi Miura[b], Satoshi Matsumura[c]

[a]*Faculty of Engineering, Hokkaido University, Kita 13, Nishi 8, Kita-ku, Sapporo 060-8628, Japan*
[b]*Faculty of Engineering, Hokkaido University, Kita 13, Nishi 8, Kita-ku, Sapporo 060-8628, Japan*
[c]*Graduate School of Engineering, Hokkaido University, Kita 13, Nishi 8, Kita-ku, Sapporo 060-8628, Japan*

Received 27 September 2013; received in revised form 20 March 2014; accepted 8 April 2014
Available online 31 July 2014

Abstract

In recent years, earthquakes and heavy rains have frequently caused soil embankments to collapse. In order to prevent the collapse of embankments, it is well known that sufficient compaction and drainage control are necessary. Although numerous research findings have described compacted soils, compaction management has been essentially based on simple parameters such as dry density, degree of saturation or air content. It is important for the construction of a stiff embankment that the effect of compaction condition on the mechanical properties and inherent anisotropy of compacted soil should be recognized in detail. In the present study, the relationships between the compaction condition and the mechanical properties obtained from laboratory tests using saturated specimens are presented. Specifically, undrained monotonic and cyclic shear strength, shear modulus, and permeability are reported. The arrangements of soil particles were also observed with a microscope. From the observation of fabric characteristics of soil particles, an inherent anisotropy of compacted soil is discussed. Furthermore, a conceptualization of the relationship between the fabric of soil particles and the mechanical characteristics for each compaction condition is suggested.

Keywords: Compaction; Soil fabric; Embankment; Undrained shear strength; Shear modulus; Permeability coefficient; D06; D09

1. Introduction

In recent years, embankment structures have frequently collapsed due to earthquakes and heavy rains. In order to prevent the collapse of embankments, it is well established that sufficient compaction of soil and drainage control is necessary.

Although all embankments initially satisfy the criterion of compaction, many embankments and structural fill become damaged over time. An example is the significant number of geo-disasters such as river embankment and residential fill collapses that occurred in the 2011 Great East Japan Earthquake (2011 Committee for Geo-hazards during Earthquakes and Mitigation Measures, 2011). Henceforth, a high quality of mechanical performance will be required for the construction of embankments that can endure various natural hazards.

In order to determine the mechanical performance of compacted embankments, basic properties such as the inherent anisotropy of compacted soil must be revealed in detail. The relationship between inherent anisotropy and shear strength

*Corresponding author.
Peer review under responsibility of The Japanese Geotechnical Society.

http://dx.doi.org/10.1016/j.sandf.2014.06.010

has been shown to contribute to improved compacted embankment design (for example, Lawton et al., 1991; Delage et al., 1996; Watabe et al., 2000; Jafari and Shafiee, 2004). Knowledge about the microstructure of compacted soil can inform rational embankment design.

A number of researchers (for example, Lambe, 1958a, 1958b; Mitchell, 1960; Seed et al., 1962; Mitchell et al., 1965 and Ahmed et al., 1974) revealed the mechanical properties of compacted clay. These researchers demonstrated that the mechanical properties of clay were significantly affected by compaction condition. In particular, Lambe (1958a, 1958b) described the effects of the differences of compaction conditions on the soil fabric and mechanical properties such as the strength, permeability, and stress–strain modulus of Boston blue clay. These findings have been useful for interpreting the effect of compaction condition on the mechanical properties of clay. For coarse-grained soil, the shear strength and deformation behavior of compacted gravel have been investigated (for example, Modoni et al., 2011). Additionally, the influence of suction on the mechanical behavior of compacted silty clay has been clarified by laboratory tests (for example, Vanapalli et al., 1999; Jotisankasa et al., 2009). Despite the many findings regarding compacted soils, for the design and construction of embankments, compaction management has been essentially based on simple parameters such as dry density, degree of saturation, or air content. In order to upgrade the construction management of embankments, the relationship between mechanical properties and compaction properties of various soils should be leveraged. Specifically, static and cyclic undrained strength, shear modulus and permeability coefficient under various compaction conditions are important for well-designed embankments. The first step of this study involved the observation of soil particles of compacted soil under a microscope. The relationships between soil fabrics and compacted conditions are discussed. Second, mechanical properties such as undrained strength, shear modulus and permeability were measured by a series of laboratory tests. The effect of dry density and water content on the mechanical properties of compacted soil is discussed. Finally, a mechanism of change in mechanical properties due to differences in compaction conditions is described in terms of the fabric characteristics of compacted soil.

2. Specimen preparation and compaction property

The tested soil was sampled in the Ikeda region, which is located in the eastern part of Hokkaido in Japan (the sampling site is shown in Fig. 1). This soil was used as a material in the construction of a river embankment. In this paper, the soil is referred to as I soil. Fig. 2 shows the grain distribution of I soil. In this figure, the density of soil particles, liquid limit, and plastic limit are also denoted. The maximum diameter is 2.0 mm. The fines content of this soil is 68.1%. The liquid limit w_L, and plastic limit w_P, are 46.8% and 34.5%, respectively. The density of soil particle ρ_s equals 2578 kg/m^3. From these data, it is recognized that I soil is categorized as sandy-silt. Fig. 3 shows the compaction curve of I soil. This compaction curve was obtained

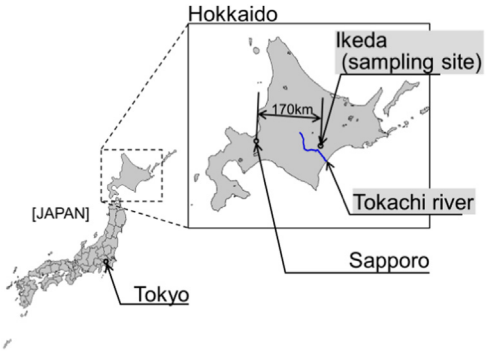

Fig. 1. Sampling location of I soil.

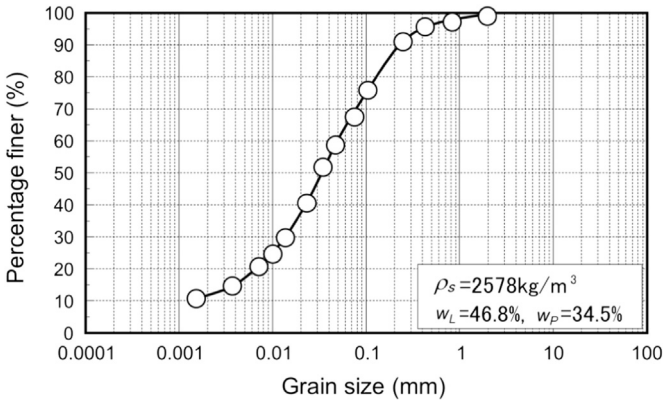

Fig. 2. Grain size distribution of I soil.

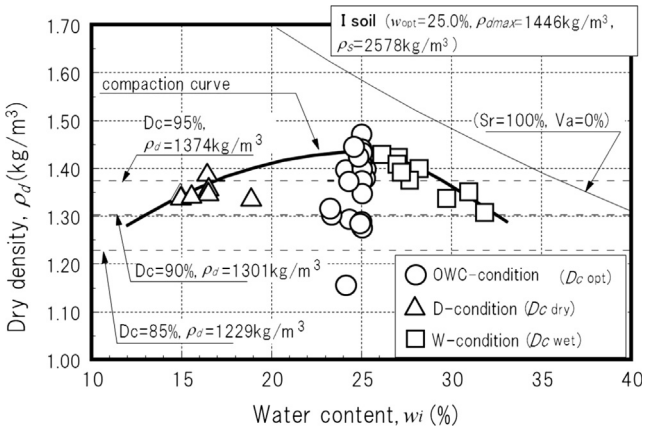

Fig. 3. Compaction curve of I soil and initial state condition of specimens.

from a compaction test with a mold that was made specifically for preparing the specimen for laboratory testing. The diameter and height of the mold were 100 mm and 150 mm, respectively. If a specimen height of over 150 mm was required for a laboratory test, compaction was performed by setting a collar on top of the mold in order to make up for the deficiency in the height of the mold. The size of the constructed mold was different from the test method defined in the ASTM standards (ASTM International, 2011). Therefore, the compaction curve for this study was derived

from the energy of 621.5 kJ/m^3, which is shown as 1.13E_c in Fig. 3. In this paper, the symbol of E_c refers to the energy value of 550 kJ/m^3, which corresponds to the compaction force of a 24.5 N rammer dropping from a height of 300 mm in the 100 mm diameter mold. Therefore, E_c is 0.917 times of the standard Proctor energy defined in the ASTM standards (ASTM International, 2011). From the compaction curve, the maximum dry density ρ_{dmax}, and the optimum water content w_{opt}, were defined as 1446 kg/m^3 and 25.0%, respectively.

In this study, the specimens were prepared through compaction of various dry densities, compaction energies and water contents. Fig. 3 also shows the initial state of specimens such as the relationship between the dry density ρ_d, and water content w_i. First, the specimens, which had various dry densities, were compacted to a near optimum water content ranging from 23% to 26%. This condition is denoted as OWC-condition in this paper. The initial situations of those specimens are illustrated by the circle markers in Fig. 3. Additionally, in order to investigate the effects of the differences of the moisture state at compaction on the mechanical behavior of compacted soil, the specimens were prepared at water content levels both above and below the optimum level. In this paper, D-condition and W-condition depict the compaction conditions at water content levels below and above the optimum level, respectively. In order to denote differences in the initial moisture state, the degree of compaction at OWC-condition, D-condition and W-condition is expressed as $D_{c\ opt}$, $D_{c\ dry}$ and $D_{c\ wet}$, respectively in Table 1.

Table 1
Initial condition of compacted specimens.

	Water content	Degree of compaction
OWC-condition	w_i=23–25% (*w_{opt}=25.0%)	$D_{c\ opt}$=80–100%
D-condition	w_i=15–19%	$D_{c\ dry}$=93–96%
W-condition	w_i=27–33%	$D_{c\ wet}$=90–100%

In preparing the specimen, the soil was compacted into the mold with various compaction energies. After removing the mold from the compacted soil, the compacted soil was formed into cylindrical specimens by trimming. Specimens with a diameter of 100 mm were prepared for the triaxial compression test and permeability test. On the other hand, following compaction work, specimens were trimmed to a diameter of 70 mm for the bender element test and the cyclic undrained test. Those specimen sizes were selected as appropriate for each test apparatus. Following compaction and trimming, the specimen was set up in the triaxial cell. After set up, the cell pressure was raised to 20 kPa in order to hold the specimen. Carbon dioxide was percolated and de-aired water was slowly

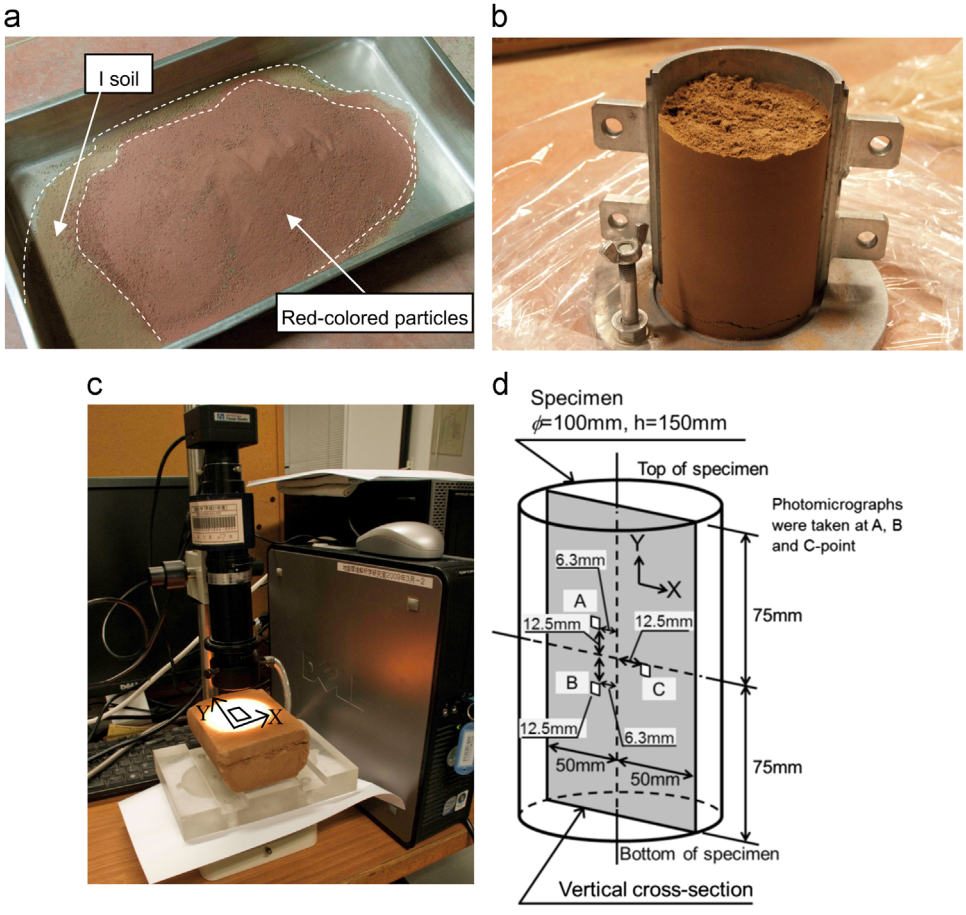

Fig. 4. Preparation and observation by digital microscope; (a) mixing red-colored particles, (b) side-view of compacted specimen, (c) situation of observation by digital microscope, (d) points of photomicrograph on the vertical cross-section of specimen.

permeated from the bottom to the top of the specimen. Thereafter, backpressure of 200 kPa was applied to saturate the specimen. Backpressure was applied until the Skempton's *B*-value reached 0.95 or above. The degree of saturation S_r of such specimens was confirmed according to the measurement of water content after testing.

3. Arrangements of soil particles

In order to see the fabric of compacted soil, cross-sectional pictures of compacted soil samples were taken by digital microscope. First, soil particles colored by red spray paint were mixed in I soil (Fig. 4(a)). The soil particles colored by red spray paint are called "red-colored particles" in this paper. Red-colored particles were targeted for observation to ascertain the arrangement of soil particles. After mixing the red-colored particles, water was sprayed onto the soil. Water contents were set to 15%, 25%, and 30%. Compaction was performed using a rammer with a weight of 24.5 N with blows of 25 times per layer for each of the 3 layers in the mold. Fig. 4(b) shows the side-view of the specimen after taking off the mold. This figure shows that the side of the specimen was not disturbed. Fig. 4 (c) shows the situation of compacted soil as observed by microscope. The photomicrographs were taken at the center of

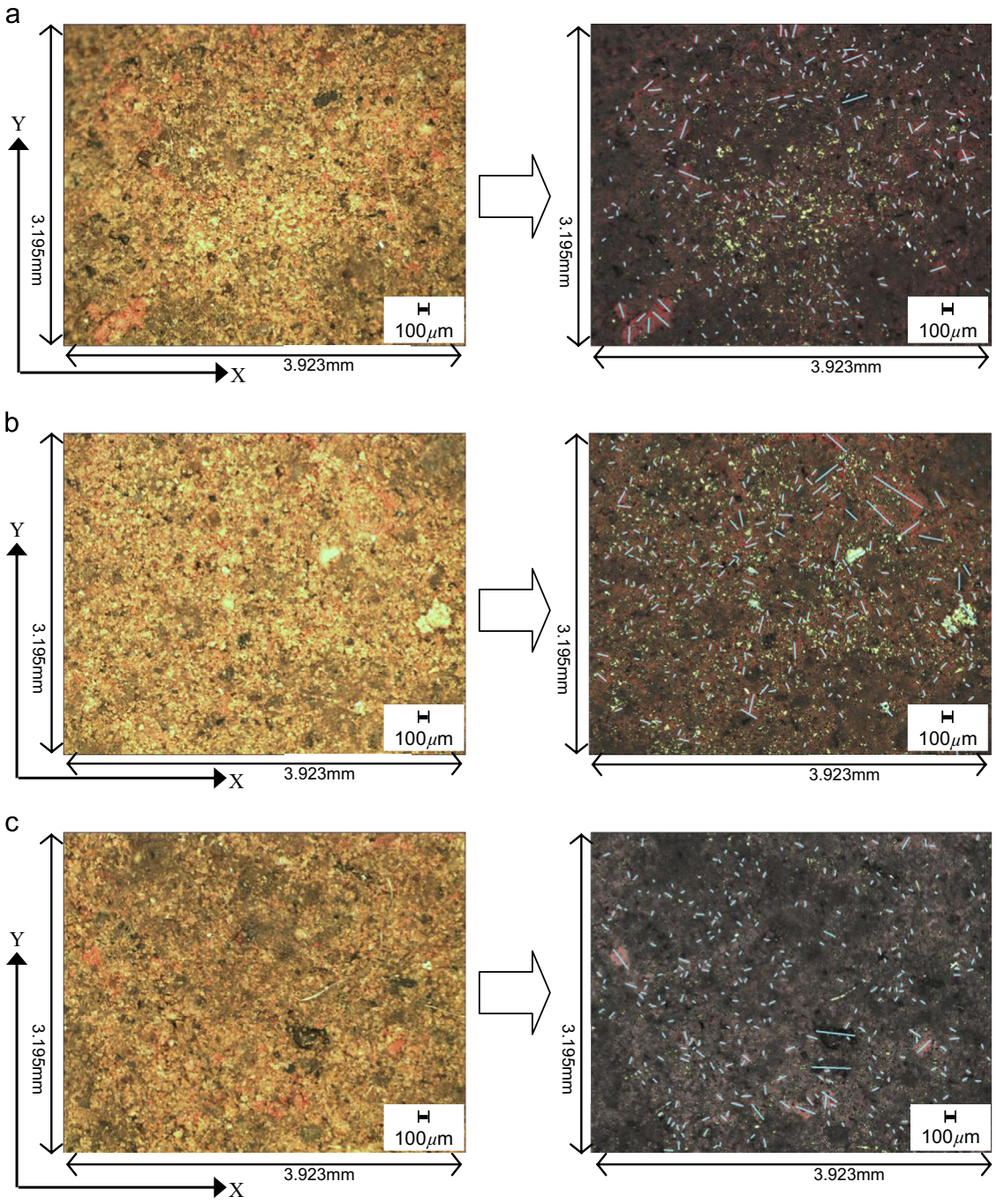

Fig. 5. Photomicrographs at the center of compacted specimen $w_i = 15\%$ (D-condition): (a) point A, red-highlighted; (b) point B, red-highlighted; (c) point C, red-highlighted.

the vertical cross-section. Three photomicrographs taken at the points *A*, *B*, and *C* are displayed below (see Fig. 4(d)). Based on the photomicrographs, the arrangements of soil particles are discussed.

Figs. 5–7 are photomicrographs at points *A*, *B*, and *C* as depicted in Fig. 4(d) at water content w_i of 15% (D-condition), 25% (OWC-condition) and 30% (W-condition), respectively. In each photograph red-colored particles can be clearly recognized. In order to observe orientation angles of soil particles, the red-colored particles were highlighted by picture processing. The long axes of red-colored particles are illustrated in those pictures.

Fig. 8 defines the orientation angle θ of a soil particle. θ indicates the orientation angle between the long axis of the soil particle and *X*-axis shown in Fig. 8. The value of θ can be taken from 0° to 180°. *S* is the length of the long axis of a soil particle.

Fig. 9(a) and (b) are rose diagrams indicating the orientation angle θ at $S < 100$ μm and $S > 100$ μm under D-condition ($w_i = 15\%$). From Fig. 9(a), it was found that θ with 60° to

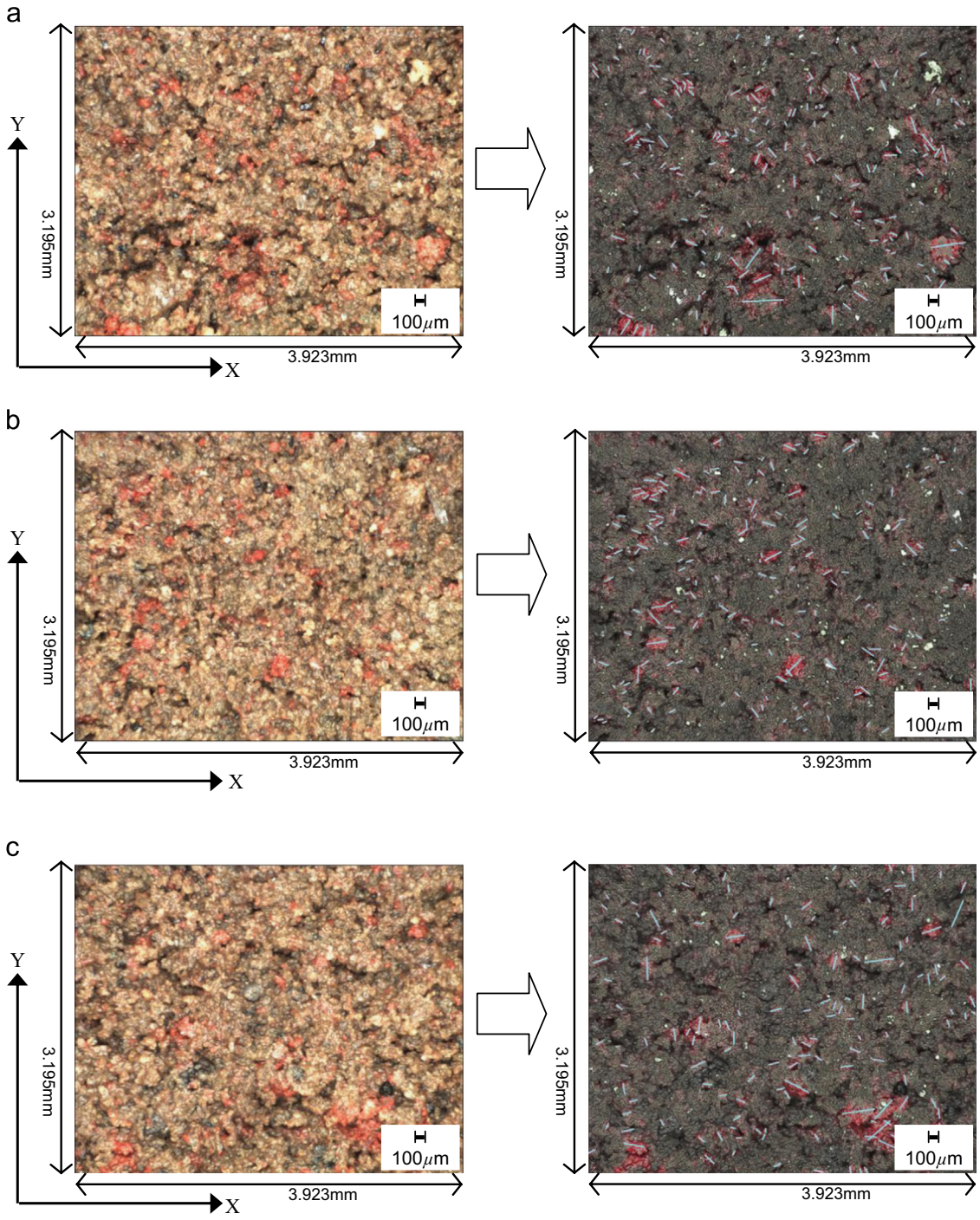

Fig. 6. Photomicrographs at the center of compacted specimen $w_i = 25\%$ (OWC-condition): (a) point A, red-highlighted; (b) point B, red-highlighted; (c) point C, red-highlighted.

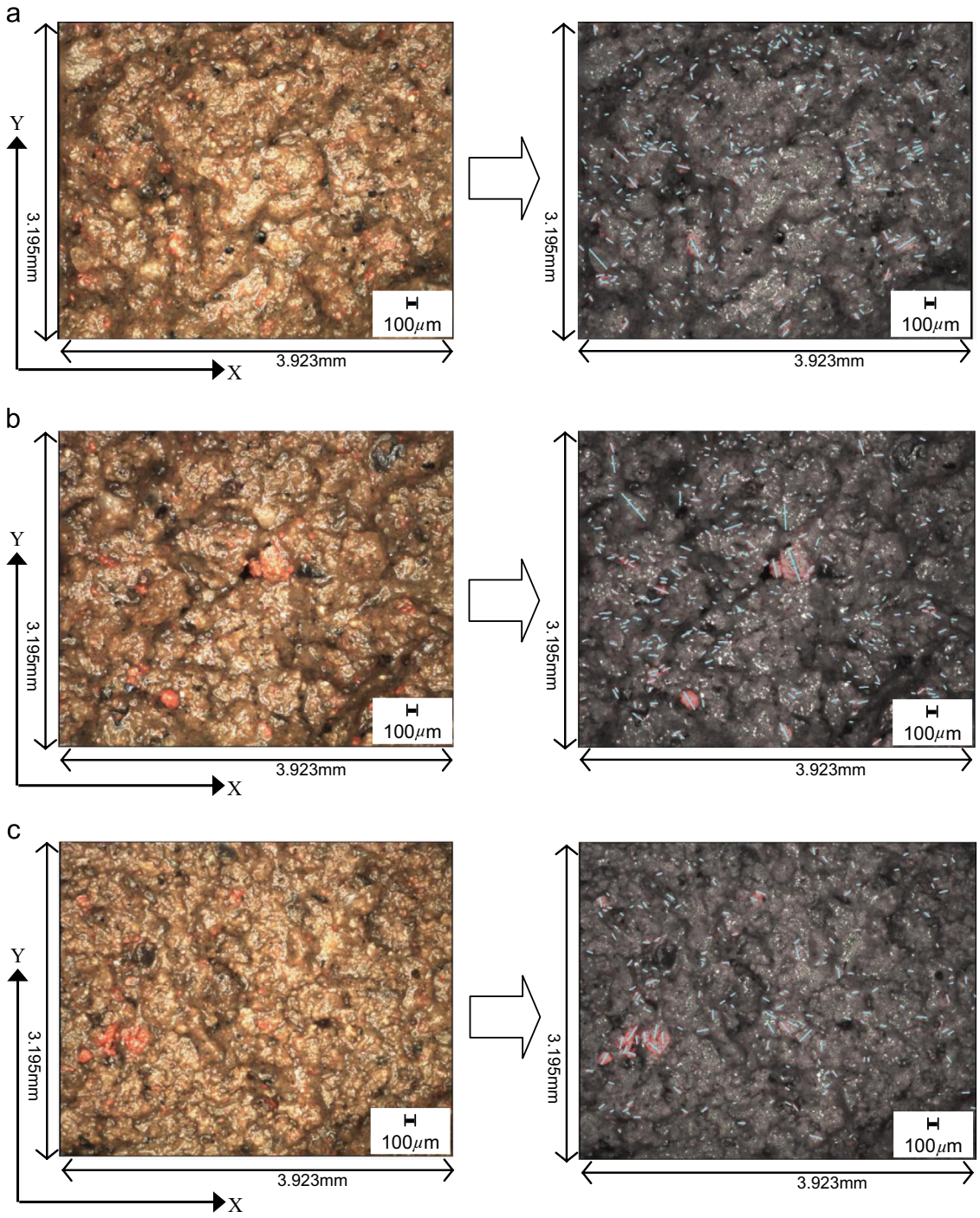

Fig. 7. Photomicrographs at the center of compacted specimen $w_i = 30\%$ (W-condition): (a) point A, red-highlighted; (b) point B, red-highlighted; (c) point C, red-highlighted.

120° was very significant $S < 100$ μm. From Fig. 9(b), it can be seen that many red-colored particles with $S > 100$ μm have a value of θ less than 30° or greater than 130°. Based on these figures, it is clear that the coarse particles are oriented in the horizontal direction and the fine particles are oriented in the vertical direction.

Fig. 10(a) and (b) also shows rose diagrams regarding θ at $S < 100$ μm and $S > 100$ μm under OWC-condition ($w_i = 25\%$). In Fig. 10(a), the values of θ of 120° to 170° of soil particles with $S < 100$ μm were slightly conspicuous. In Fig. 10(b), for soil particles with $S > 100$ μm, the values of θ were taken evenly from 0° to 180°. At OWC-condition, trends regarding soil particle orientation cannot be recognized.

Fig. 11(a) and (b) are rose diagrams for θ at $S < 100$ μm and $S > 100$ μm under W-condition ($w_i = 30\%$). Within these figures, different trends from the D- and OWC-condition (see Figs. 9 and 10) can be observed. It can be seen in Fig. 11(a) that the values of θ of small particles ($S < 100$ μm) were near horizontal (i.e., $\theta < 30°$ or $\theta > 130°$). On the other hand, Fig. 11 (b) shows that θ for many soil particles with $S > 100$ μm was

90° to 130°. From these figures, it is evident that the coarse particles are oriented in the vertical direction and the fines particles are oriented in the horizontal direction. The orientation of soil particles under W-condition corresponds to the inverse pattern at D-condition. From these observations, it can be deduced that the arrangements of soil particles are affected by the water content at compaction under the same compaction energy.

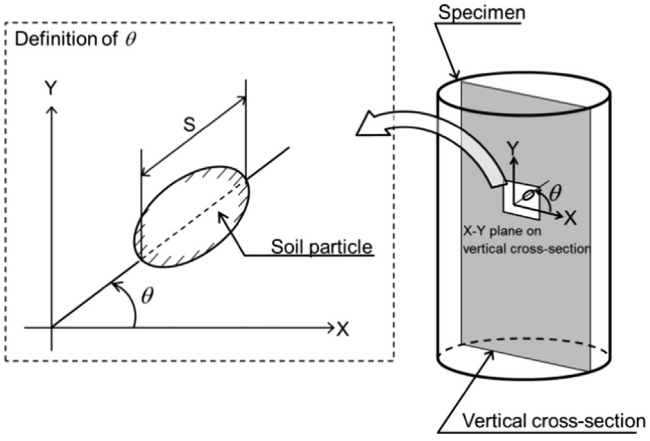

Fig. 8. Definition of orientation angle of a soil particle.

4. Test procedures

The mechanical behavior of each compacted specimen was investigated by conducting a consolidated undrained triaxial compression test (CU test), a bender element test, a permeability test and a cyclic undrained triaxial test. First, the axial load on the CU test was applied with a speed of 0.1%/min in axial strain. The specimens were 150 mm in height and 100 mm in diameter. The effective confining pressure σ'_c was selected at 50 kPa, 100 kPa and 150 kPa. The bender element tests were performed at the effective confining pressure σ'_c of 50 kPa with the test apparatus shown in Fig. 12(a). Specimens that were 70 mm in diameter and 150 mm in height were used. After consolidation, the shear wave velocity was measured by a pair of bender elements, which were attached on the top-cap and pedestal of the test apparatus. The shear wave velocity V_s, and shear modulus G_{BE}, can be determined as follows;

$$V_s = L/t \tag{1}$$

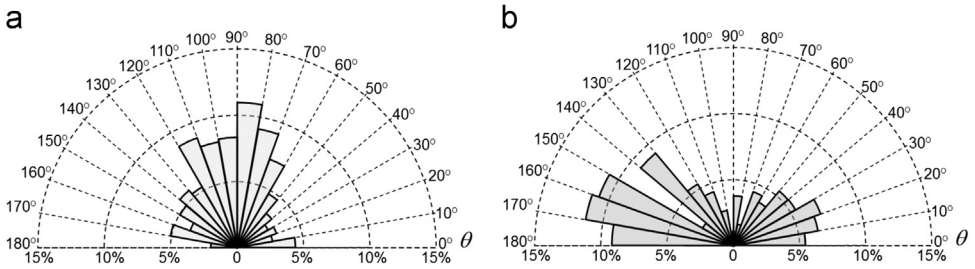

Fig. 9. Rose diagrams about orientations of soil particles (D-condition); (a) $S < 100$ μm, (b) $S > 100$ μm.

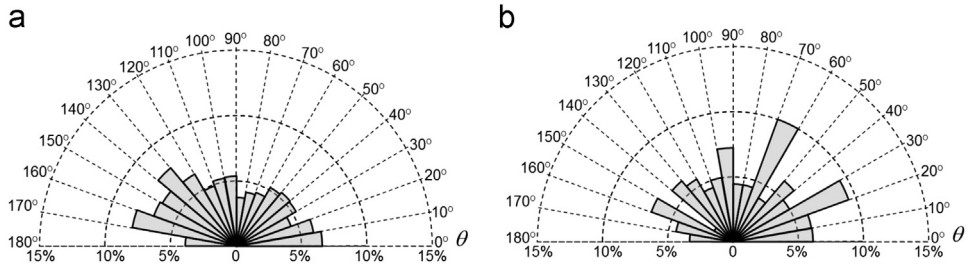

Fig. 10. Rose diagrams about orientations of soil particles (OWC-condition); (a) $S < 100$ μm, (b) $S > 100$ μm.

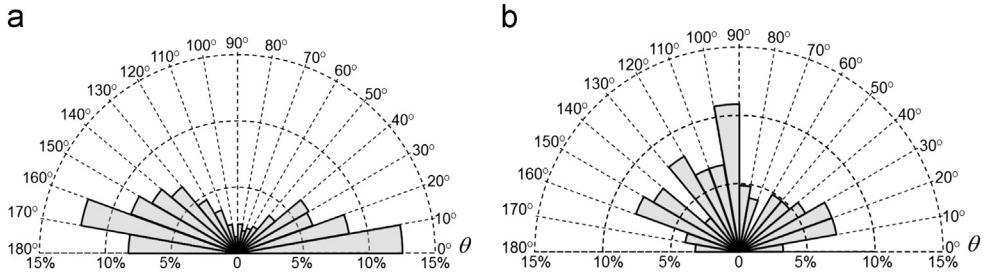

Fig. 11. Rose diagrams about orientations of soil particles (W-condition); (a) $S < 100$ μm, (b) $S > 100$ μm.

$$G_{BE} = \rho_t V_s^2 \quad (2)$$

where L is the effective distance traveled by the shear wave through the specimen; t is the traveling time of the shear wave; and ρ_t is the density of the specimen (Sahaphol et al., 2005; Sahaphol and Miura, 2005). In this study, a series of falling head permeability tests were performed by means of the apparatus shown in Fig. 12(b). The test apparatus had two burettes, which were connected to the specimen through tubes, and could make a difference in the water head level between the top and bottom of the specimen. The elapsed time of the permeability test and volume of water through the specimen were recorded. In order to obtain the permeability coefficient under saturated conditions, a backpressure of 200 kPa was supplied into the specimen. Before measuring the permeability coefficient, the specimen was consolidated at the effective confining pressure of 50 kPa. For the cyclic undrained triaxial test (JGS0541-2009), cyclical axial loading at a frequency of 0.1 Hz was applied to the specimen with positive and negative amplitude being kept constant during loading. The cyclic loading was continued until the double amplitude of axial strain *DA* reached 10%.

5. Results and discussions

5.1. Undrained shear strength

Fig. 13(a) and (b) shows the relationships between deviator stress $\sigma'_1 - \sigma'_3$, and axial strain ε_a, at effective confining stresses σ'_c of 50 kPa and 150 kPa, respectively. σ'_1 and σ'_3 are major and minor effective principal stresses. From these figures, it can be observed that the shapes of the deviator stress–axial strain curves until the axial strain reaches 0.1% and are very similar to each compaction condition at σ'_c of 50 kPa and 150 kPa. Therefore, the shear modulus at small strain levels were observed closely by a series of bender element tests described below. In the condition of compaction energy of $1.13E_c$, it was found that the maximum value of deviator stress at $D_{c\ opt}$ of near 100% was higher than those of the other cases. From Fig. 13(a), it is recognized that the condition of compaction varies the magnitude of shear strength even though the degree of compaction was within the range of 88.3% to 93.5%. At D-condition, the peak of deviator stresses appeared at the axial strain ε_a of near 1%. At OWC-condition, the peak of deviator

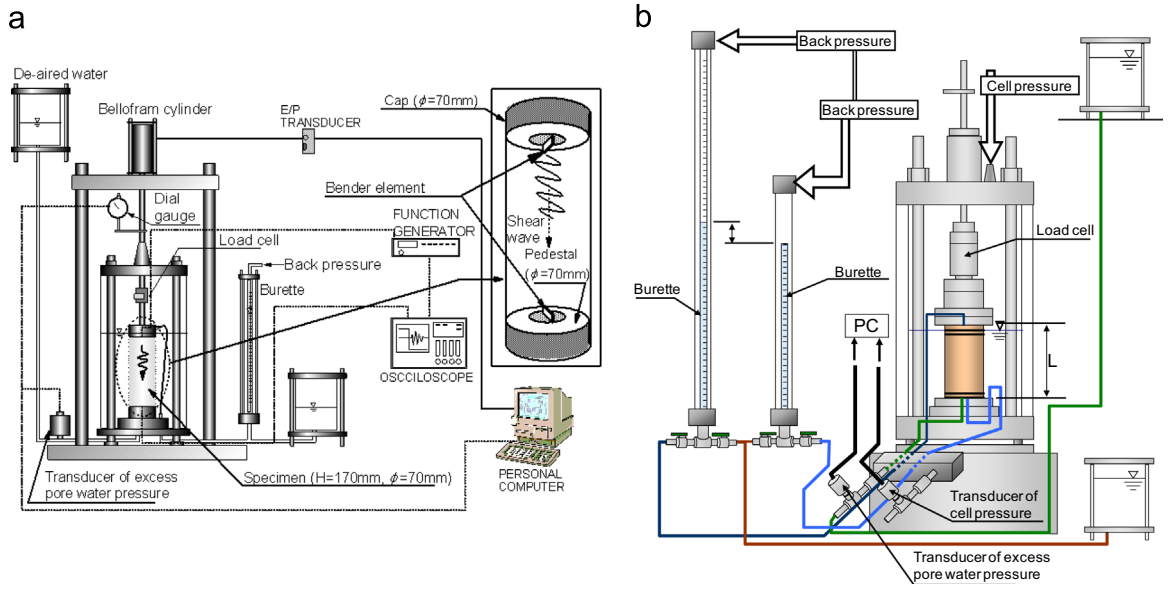

Fig. 12. Test apparatus; (a) bender element test, (b) permeability test.

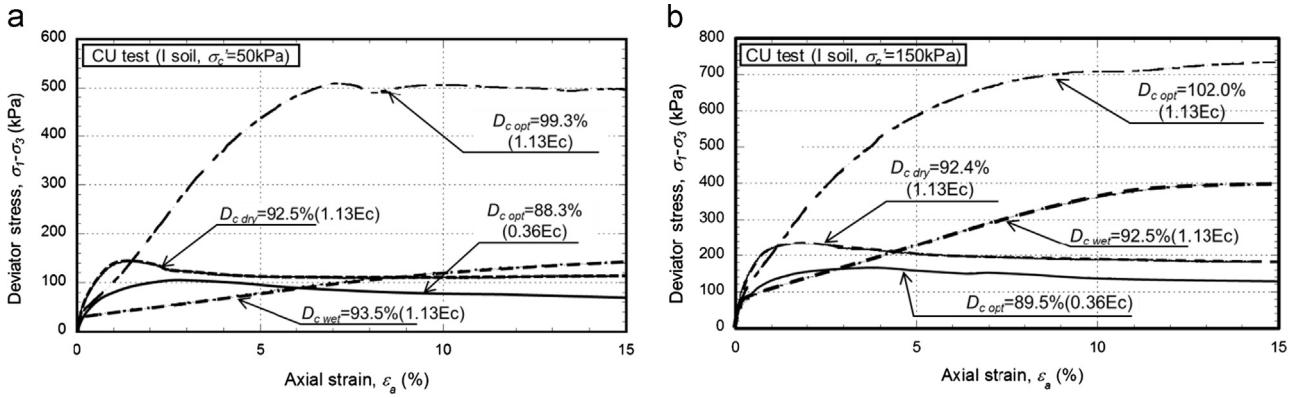

Fig. 13. Stress–strain curves obtained from CU test; (a) σ'_c of 50 kPa, (b) σ'_c of 150 kPa.

stress seems to appear at near 2.5% of axial strain. The magnitude of peak stress is smaller than that of D-condition. On the other hand, at W-condition, it is evident that the values of deviator stresses at a small strain level, which is less than 5%, were smaller than that of D-condition. Fig. 13(b) denotes the results of CU tests at σ'_c of 150 kPa. From this figure, it can be observed that the tendency of the relationship between deviator stress and axial strain is similar to the results at σ'_c of 50 kPa shown in Fig. 13(a). Specifically, the deviator stress at $D_{c\ opt}$ of 102% is demonstratively higher than those of the compacted specimens with the compaction energy of $1.13E_c$. These results indicate that compaction under the optimum water content is successful in producing higher shear strength in compacted embankments. Next, the effect of water content at compaction on shear strength can be seen among the results of $D_{c\ opt}$ of 89.5%, $D_{c\ dry}$ of 92.4% and $D_{c\ wet}$ of 92.5%. This figure indicates that until the axial strain reaches 3%, the deviator stress at $D_{c\ dry}$ of 92.4% is greater than those of $D_{c\ opt}$ of 89.5% and $D_{c\ wet}$ of 92.5%. Additionally, the peak of the deviator stresses of OWC-condition and D-condition appear when the axial strain is near 3%. In contrast, the deviator stress of W-condition does not show its peak under an axial strain of 15%. These results appear to indicate the compaction condition affects the undrained shear strength properties of compacted soils.

Fig. 14 shows the relationship between peak strength, q_{max} and the degree of compaction, D_c. q_{max} is defined as the maximum value of deviator stress, $\sigma'_1-\sigma'_3$. If q_{max} cannot be determined in the stress–strain curve, q_{max} is defined as the deviator stress at the axial strain of 15%. In this figure, the solid line expresses the trend of q_{max} under compaction at OWC-condition and σ'_c of 50 kPa. At σ'_c of 50 kPa, it can be observed that the magnitude of q_{max} at OWC-condition is higher than with other conditions. At σ'_c of 100 kPa, the effect of differences in water content w_i on the relationship between q_{max} and D_c is not significant. Finally, at σ'_c of 150 kPa, q_{max} at D-condition is slightly smaller than in the other cases. In this figure, the data at $D_{c\ opt}$ of 102% was obtained through consolidation. Though the reason for the data at $D_{c\ opt}$ appearing over 100% has yet to be clarified, similar trends in the relationships between q_{max} and water content w_i, were also observed in test results using volcanic soil sampled in Sapporo, Japan (Ito et al., 2012). In general, it has been recognized that the shear strength or the deviator stress required to achieve about 5% of the strain at drier conditions is higher than that of wetter conditions (Mitchell et al., 1965). In the present study, it is hypothesized that similar results for the relationship between deviator stress at small strain and water content can be expected.

In order to depict the deformation behavior of I soil, the relationship between the axial strain at failure ε_f and the degree of compaction D_c, is shown in Fig. 15. ε_f is defined as the axial strain at which q_{max} appears. The solid line highlights the data pertaining to the OWC-condition. The figure demonstrates that the magnitude of ε_f increases with an increase in $D_{c\ opt}$ under the OWC-condition. At 90% and 100% of $D_{c\ opt}$, the values of ε_f reach 3.5% and 11%, respectively. Undert the D-condition, the values of ε_f are smaller than those of the other cases. On the other hand, for the W-condition, the axial strain ε_f appears larger than those of the other cases. In particular, the values of ε_f reach nearly 15% under the W-condition. It is hypothesized that the axial strain at q_{max} varies because the fabric of soil depends on the compaction condition.

Figs. 16 and 17 illustrate the relationships between q_{max} and water content or compaction energy ratio E_{ci}/E_c at σ'_c of 50 kPa and 150 kPa, respectively. E_{ci} indicates the compaction energy for each specimen. Fig. 16 demonstrates that q_{max} increases with an increase in D_c or E_{ci}/E_c at OWC-condition. Additionally, it can be observed that q_{max} under the D- and W-conditions are smaller than the value under the OWC-condition, even though the compaction energy ratio E_{ci}/E_c reaches 1.13. In order to examine the strength of compacted soil under high confining pressure, Fig. 17(a) and (b) shows the values of q_{max} at σ'_c of 150 kPa. Fig. 17(a) demonstrates that q_{max} reaches its maximum value at a $D_{c\ opt}$ of 102.0% and w_i of 25%. If specimens had a D_c of 93%, q_{max} at w_i of 29.7% was higher than that at the optimum water content. Further, Fig. 17 (b) shows that q_{max} increases with an increase in E_{ci}/E_c. The values of q_{max} under the D- and W-condition at E_{ci}/E_c of 1.13 were smaller than that under the OWC-condition at E_{ci}/E_c of 1.13. These results indicate that the undrained shear strength of compacted soil is strongly affected by compaction energy, water content and confining pressure.

Fig. 18(a)–(c) displays the effective stress paths as $p'/\sigma'_c-q/\sigma'_c$ relations under the OWC-, D- and W-condition, respectively. p' is the effective mean principal stress $((\sigma'_1+2\sigma'_3)/3)$, q is the deviator

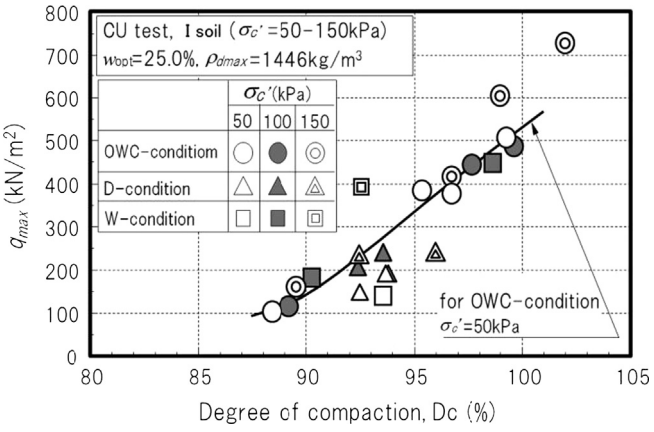

Fig. 14. Relationship between peak strength and degree of compaction.

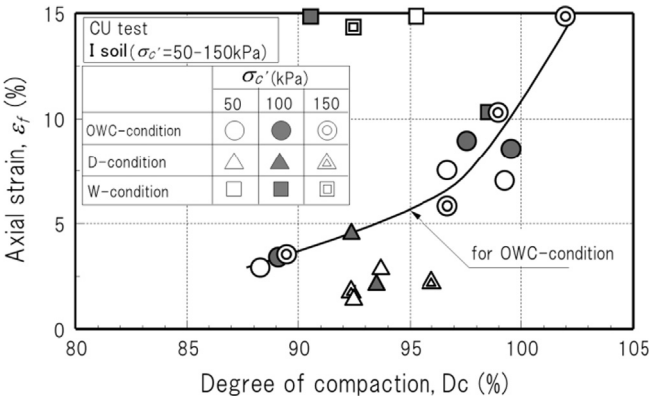

Fig. 15. Relationship between axial strain at failure and degree of compaction.

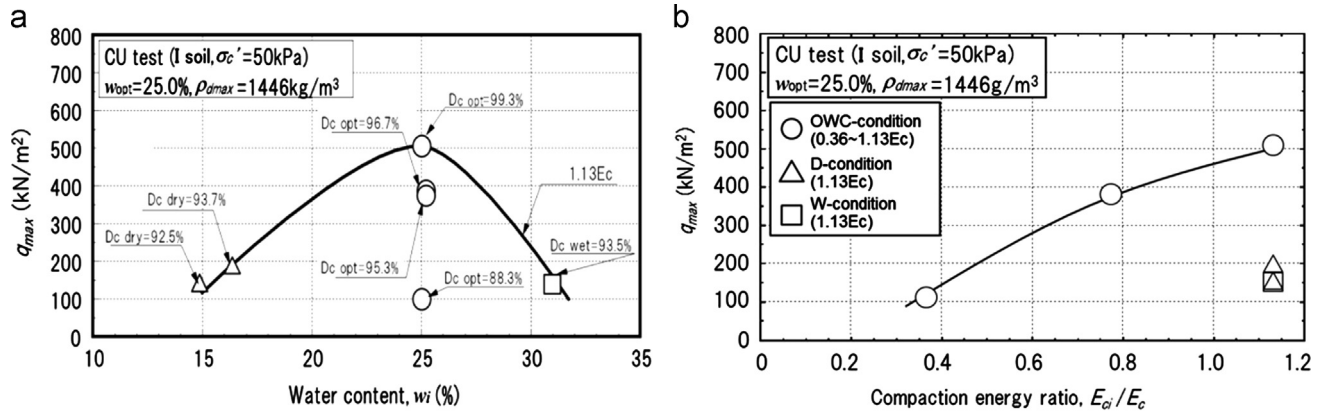

Fig. 16. Peak strength q_{max} at σ'_c of 50 kPa; (a) effect of water content, (b) effect of compaction energy ratio.

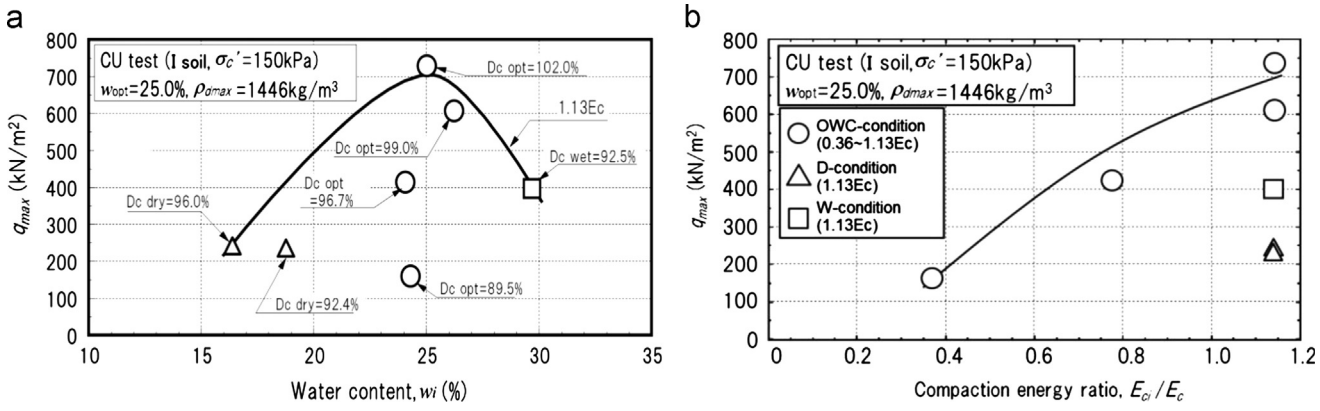

Fig. 17. Peak strength q_{max} at σ'_c of 150 kPa; (a) effect of water content, (b) effect of compaction energy ratio.

stress $(\sigma'_1-\sigma'_3)$, and σ'_c is the effective confining pressure. These figures denote the results on the degree of compaction D_c of about 90%. Fig. 18(a) shows that the value of q/σ'_c and p'/σ'_c reaches 2.1 and 1.4 in the case of σ'_c of 50 kPa. After q/σ'_c reached its peak, it can be seen that both p'/σ'_c and q/σ'_c decrease until the end of the undrained shear test. In the cases of $\sigma'_c$of 100 kPa and 150 kPa, p'/σ'_c becomes about 0.8 at which q/σ'_c reached the peak value of 1.2. Fig. 18(b) illustrates that p'/σ'_c increases with an increase in q/σ'_c at the case of σ'_c of 50 kPa and 100 kPa. For σ'_c of 150 kPa the value of p'/σ'_c reduced to only 0.8, which is more conservative than that under the OWC-condition. Next, Fig. 18(c) demonstrates that the pattern of effective stress change is quite different from the OWC- and D-conditions. It can be observed at σ'_c of 50 kPa that p'/σ'_c immediately reduces the value from 1.0 to 0.7, thereafter p'/σ'_c continues to increase the value until the end of the shear test. In the cases of the other confining pressures, a similar behavior can be recognized under the W-condition. It can be posited that the effective mean principal stress decreases more easily from undrained compression than under the OWC- and D-conditions. This indicates that the dilation behavior of compacted soil is significantly affected by differences in compacted condition.

5.2. Permeability coefficient

The permeability coefficients of compacted soil are illustrated as the relationships among the permeability coefficient k, degree of compaction D_c, and compaction energy ratio E_{ci}/E_c, in Fig. 19(a) and (b). These figures show that the permeability coefficient, k decreases with an increase in D_c and E_{ci}/E_c. The permeability coefficient k under the drier condition at $D_{c\ \mathrm{dry}}$ of 96% was higher than in the other cases with the same degree of compaction. The results indicate that compaction at the drier condition made vertical permeability high. In a contrasting situation, at the wetter condition compaction resulted in low vertical permeability of the soil fabric.

Fig. 20 illustrates the relationship between permeability coefficient k, and the water content, w_i. Results under a compaction energy of $1.13E_c$ are highlighted by a solid line in this figure. It can be observed that the permeability coefficient k at the water content of 18% (D-condition) reached about five times of the value under the OWC-condition. When the water content was 27% (W-condition), the value of k was similar to that of the optimum water content. These results illustrate that water content can be an important parameter in controlling the permeability of compacted soil. On the other hand, focusing on the difference of $D_{c\ \mathrm{opt}}$, the permeability coefficient k significantly decreased with an increase in $D_{c\ \mathrm{opt}}$. These results suggest that the permeability coefficient and void shape in compacted soil are also affected by the compaction condition in terms of the degree of compaction and water content.

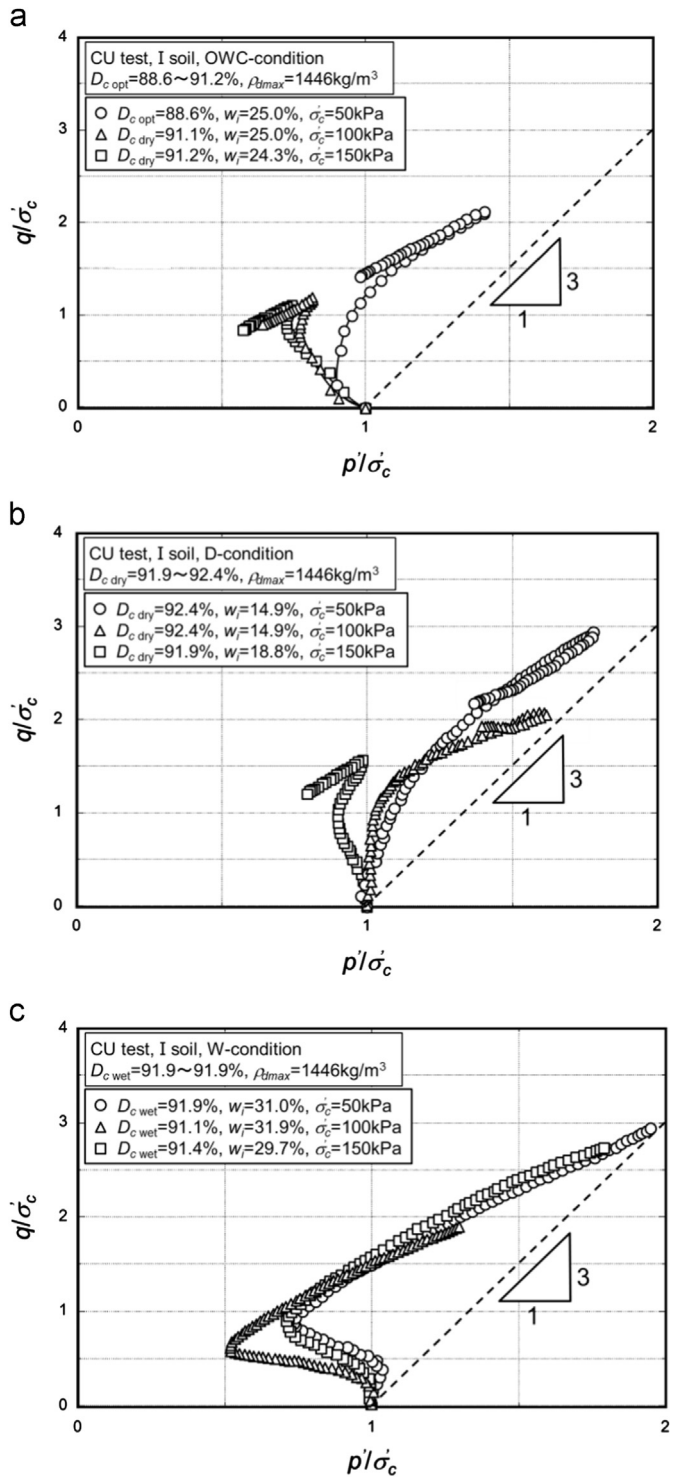

Fig. 18. Normalized effective stress paths obtained from CU test; (a) OWC-condition, (b) D-condition, (c) W-condition.

5.3. Small strain shear modulus

Fig. 21(a) and (b) illustrates the relationships between the shear modulus G_{BE}, degree of compaction D_c, and compaction energy ratio E_{ci}/E_c. These figures show that the shear modulus, G_{BE} increases with an increase of D_c and E_{ci}/E_c. A similar tendency for various sands was observed in bender element tests (for example, Gu et al., 2013; Senetakis et al., 2013). Additionally, G_{BE} obtained from the specimen at $D_{c\ wet}$ with 96 to 97% seem a little higher than those of the other cases. Fig. 22 denotes the relationship between G_{BE} and water content at compaction w_i. Within this figure it can be seen that the peak values of G_{BE} did not appear at the optimum water content under the compaction energy of $1.13E_c$. The value of G_{BE} at w_i of 27% was slightly greater than that of the specimen at $D_{c\ opt}$ of 100%. Under unsaturated conditions, it is well known that the shear modulus at conditions drier than the optimum water content is higher due to the suction effects. Furthermore, the shear modulus increases with an increase in soil suction (Runigo et al., 2009; Sawangsuriya et al., 2008; Heitor et al., 2013). On the other hand, the shear modulus under the saturated condition has been indicated in this paper. Therefore, it appears that the shear modulus D- and OWC-conditions would be higher than those shown in the present paper if the tests were performed under unsaturated conditions. This result illustrates that specimen stiffness is affected by the degree of compaction and water content at compaction. In addition, it can be recognized that the maximum value of G_{BE} may appear at a slightly wetter condition than the optimum water content.

5.4. Cyclic undrained strength

Fig. 23(a)–(c) shows the effective stress paths obtained from the cyclic undrained tests at OWC-, D- and W-condition, respectively. σ_d is the deviator stress $(\sigma'_1-\sigma'_3)$ and p' is the effective mean principal stress. The specimens have a degree of compaction, D_c, of near 93%. The cyclic stress ratio $\sigma_d/2\sigma'_c$ ranges from 0.266 to 0.321. The effective confining stress σ'_c was set to 50 kPa. Fig. 23(a) shows that the effective mean principal stress p' gradually decreases from an initial value of p' of 50 kPa at the beginning of cyclic loading. Under the D-condition, the behavior of p' was similar to under the OWC-condition (Fig. 23(b)). On the contrary, Fig. 23(c) demonstrates that under the W-condition p' decreases more significantly at the beginning of cyclic loading than in the other cases. These results indicate that the difference in the compaction condition varies the behavior of effective mean principal stress p'. In other words, it may indicate that the behavior of excess pore water pressure depends significantly on the difference of compaction conditions.

Fig. 24(a)–(c) shows the relationships between the cyclic stress ratio $\sigma_d/2\sigma'_c$, and the number of loading cycles N_c, at double amplitude of axial strain DA of 5%. Fig. 24(a) illustrates that the cyclic strength increases with an increase in $D_{c\ opt}$. In the case of $D_{c\ opt}$ with 95 to 100%, SR_{20}, which is defined as the cyclic stress ratio at N_c of 20, is about 1.8 times higher than those of $D_{c\ opt}$ with 85% to 90%. The relationship between the cyclic stress ratio and N_c at D-condition is shown in Fig. 24(b). In this figure, the cyclic strength of the D-condition appears higher than that of the OWC-condition, as shown in Fig. 24(a). It should be noted that the effect of the degree of compaction on the cyclic strength under low water content condition at compaction is more significant than that at the optimum water content condition. Next, Fig. 24(c) shows the relationship between the cyclic stress ratio and N_c under the

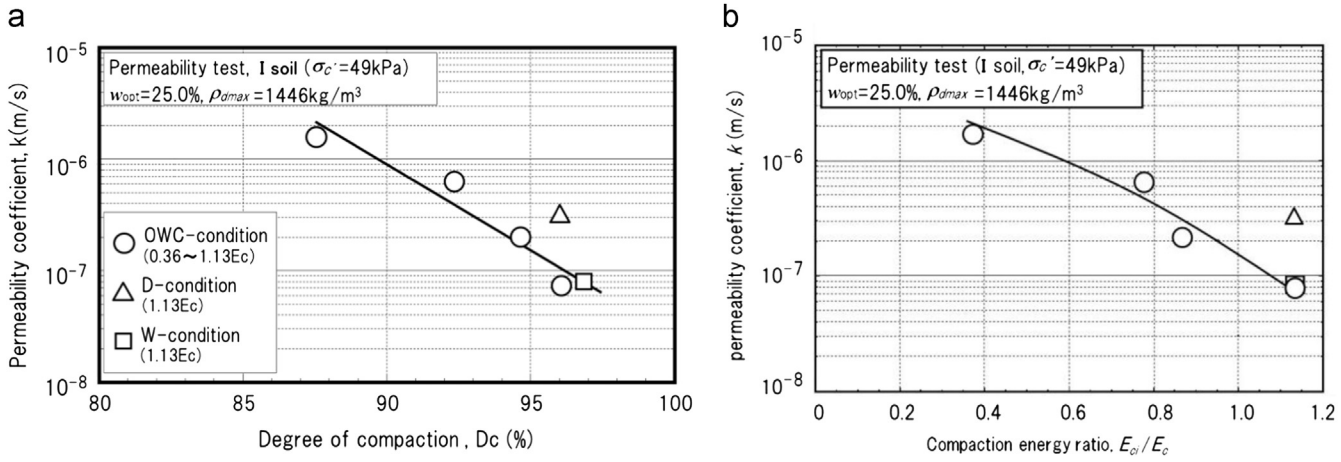

Fig. 19. Permeability coefficient; (a) effect of degree of compaction, (b) effect of compaction energy ratio.

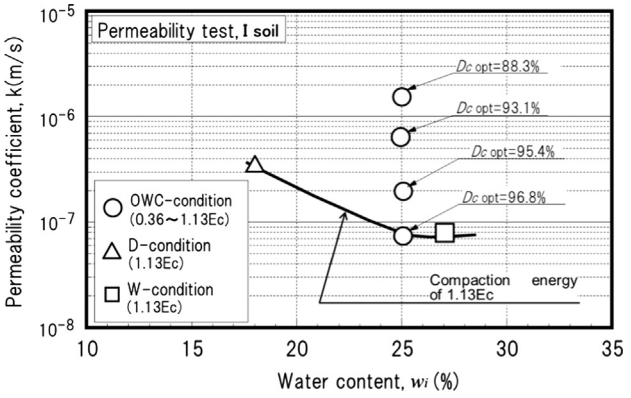

Fig. 20. Relationship between permeability coefficient and water content at compaction.

W-condition. This figure indicates that the difference between the value of SR_{20} of 95–100% in $D_{c\ wet}$, and that at 90–95% in $D_{c\ wet}$, is very small. Though the specimen has a high degree of compaction, it appears difficult to achieve high cyclic strength through compaction under wetter conditions.

Fig. 25 shows the relationship between the cyclic strength SR_{20} and the degree of compaction D_c. This figure reveals that the SR_{20} increases with an increase in D_c. The rate of cyclic strength increase against D_c under the D-condition is higher than in the other cases. On the other hand, the values of SR_{20} are rarely influenced by the degree of compaction within the range of 92% to 97% under the W-condition. The experimental findings reveal that the cyclic strength of compacted soil is affected by the degree of compaction and the water content at compaction. It appears that compaction under drier conditions can be beneficial for cyclic undrained strength.

5.5. Relationship among undrained strength, shear modulus and permeability

The effects of suction on the mechanical behavior of compacted soil have been examined in a number of studies (for example, Tarantino and Tombolato, 2005; Thu et al., 2007; Taibi et al., 2011). Based on this research, it has been recognized that compaction under dryer conditions provides high suction, shear strength and stiffness. While the study of mechanical behavior in reference to the suction effect is important, the characteristics of saturated conditions are also important in predicting failure behavior as the mechanical state of soils is more unfavorable at the saturated state. This is also important for engineering design as the shear modulus and permeability coefficient are related to the inherent anisotropy and undrained strength or cyclic strength at saturated conditions. In order to reveal the mechanical properties of compacted soil, the relationships among undrained strength, cyclic strength, shear modulus and permeability coefficient need to be examined in detail. Table 2 shows a list of test results for q_{max}, k/k^*, G_{BE}/G^*_{BE} and SR_{20}/SR^*_{20}. k^*, G^*_{BE} and SR^*_{20} are k, G_{BE} and SR_{20} at $D_{c\ opt}$ of 97%, respectively. Based on Table 2, the effects of differences in compaction condition on the mechanical properties of soil are discussed.

Fig. 26(a) and (b) expresses the relationships among q_{max}, G_{BE} and k obtained from a series of laboratory tests. Fig. 26(a) illustrates the relationship between q_{max} and k/k^*. This figure shows that the value of q_{max} decreases with an increase of k/k^*. Under the same compaction energy, the magnitudes of q_{max} at $D_{c\ dry}$ or $D_{c\ wet}$ of 95% are equal to half of that at $D_{c\ opt}$ of 97%. At $D_{c\ dry}$ of 95%, the value of k/k^* is about 4 times higher than that at $D_{c\ opt}$ of 97%. On the other hand, the value of k/k^* at $D_{c\ wet}$ of 95% is similar to that at $D_{c\ opt}$ of 97%. Fig. 26(b) shows the relationship between q_{max} and G_{BE}/G^*_{BE}. This figure demonstrates that q_{max} increases with an increase of G_{BE}/G^*_{BE} at OWC-condition. On the other hand, the values of G_{BE}/G^*_{BE} under the D-condition and W-condition with $D_{c\ dry}$ or $D_{c\ wet}$ of 95% are 0.87 and 1.17, respectively. Both sets of data show that the relationship between q_{max} and G_{BE}/G^*_{BE} are affected by water content even if the degree of compaction are the same. This indicates that undrained strength is related to the permeability and the shear modulus of compacted soil.

Fig. 27(a) shows the relationship between SR_{20}/SR^*_{20} and k/k^*. This figure illustrates that SR_{20}/SR^*_{20} decreases with an increase in the k/k^* under the OWC-condition. Under the D-condition, SR_{20}/SR^*_{20} and k/k^* at $D_{c\ dry}$ of 95% are 1.15 and 4.2, respectively. The value of SR_{20}/SR^*_{20} of the D-condition is higher than that of the OWC-condition at a k/k^* of 4.2. On

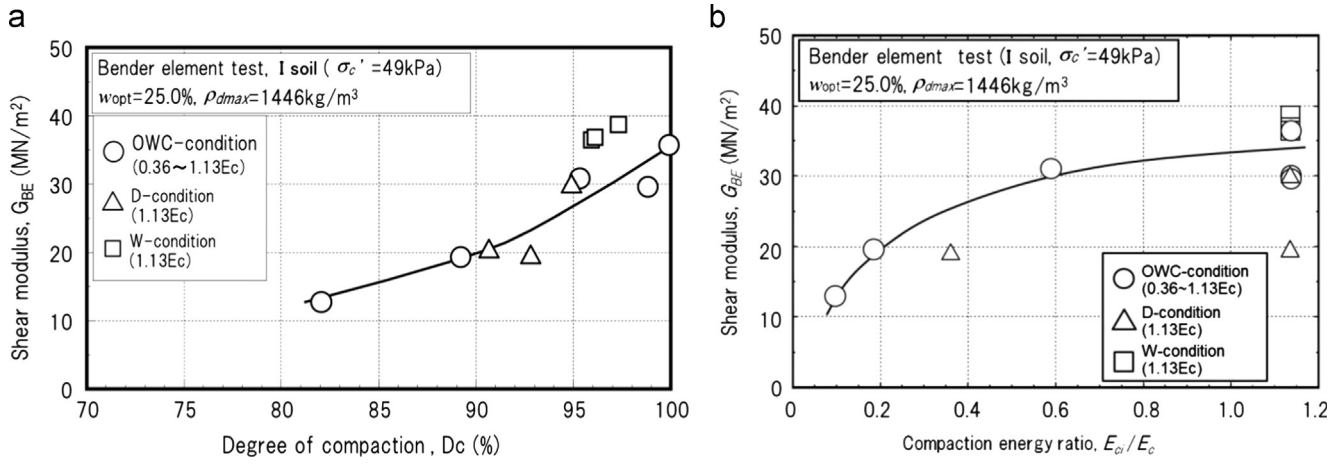

Fig. 21. Shear modulus; (a) effect of degree of compaction, (b) effect of compaction energy ratio.

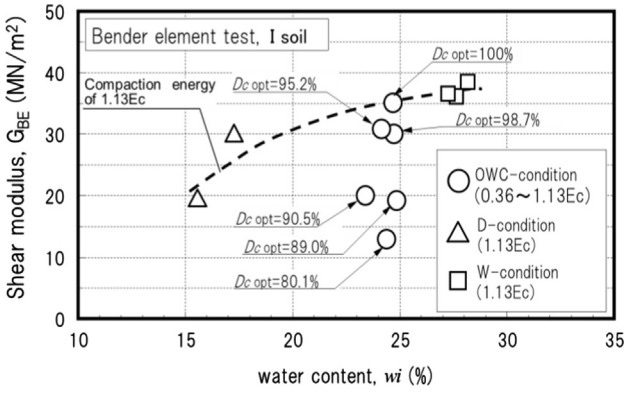

Fig. 22. Relationship between shear modulus and water content at compaction.

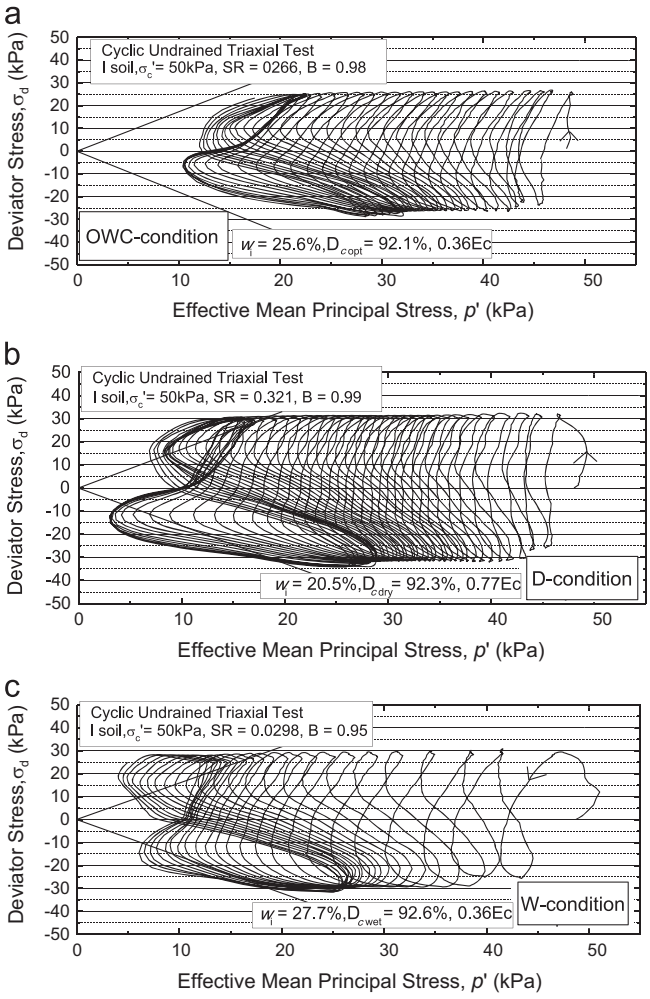

Fig. 23. Effective stress paths obtained from the cyclic undrained tests; (a) OWC-condition, (b) D-condition, (c) W-condition.

the contrary, under the wetter condition, SR_{20}/SR^*_{20} and k/k^* at $D_{c\ wet}$ of 95% are 0.75 and 1.1, respectively. The value of SR_{20}/SR^*_{20} at W-condition is less than that of the OWC-condition at a k/k^* of 1.1. The results appear to indicate that the relationships between the cyclic strength and permeability are affected by the water content at compaction. The cyclic undrained strength under drier conditions is higher than those of wetter and optimum water content conditions, even if the values of the permeability coefficient are the same. Fig. 27(b) illustrates the relationship between SR_{20}/SR^*_{20} and G_{BE}/G^*_{BE}. The figure indicates that SR_{20}/SR^*_{20} increases with an increase in G_{BE}/G^*_{BE} at OWC-condition. In spite of about 0.8 of G_{BE}/G^*_{BE}, the magnitude of SR_{20}/SR^*_{20} at $D_{c\ dry}$ of 95% is greater than that of $D_{c\ opt}$ of 97%. On the contrary, SR_{20}/SR^*_{20} at $D_{c\ wet}$ of 95% is less than that of $D_{c\ opt}$ of 97%. The cyclic undrained strength of compacted sandy silt seems to be strongly influenced by differences in compaction condition such as water content even if the degrees of compaction are the same.

5.6. Relationships between mechanical property and inherent fabric of compacted soil

The effect of the inherent fabric and anisotropy on the mechanical properties of various soils has been investigated by many researchers. For example, Lambe (1958a, 1958b) and Onitsuka et al. (1979) described the relationship between the arrangement of soil particles and the mechanical properties of compacted clay. Ahmed et al. (1974) revealed that the pore size distribution and unconfined peak strength of clay were affected by the water content at compaction and compaction

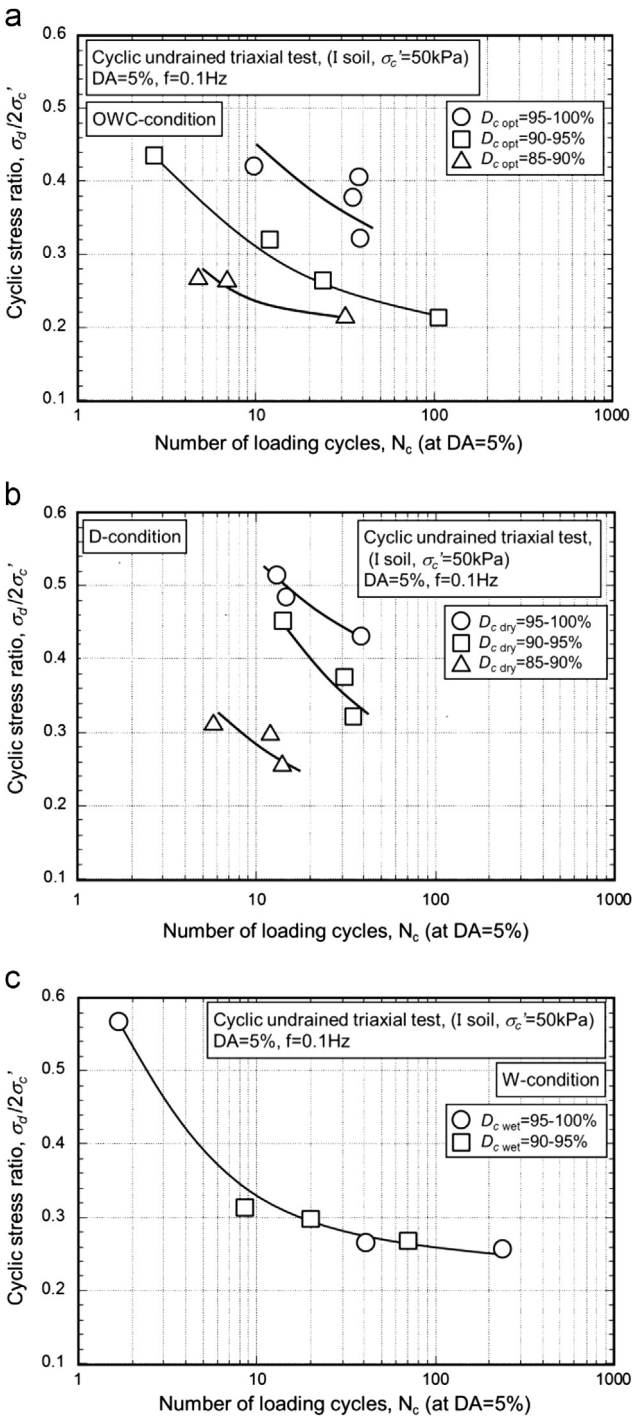

Fig. 24. Relationships between the cyclic stress ratio and number of loading cycles; (a) OWC-condition, (b) D-condition, (c) W-condition.

method. Vanapalli et al. (1999) described the soil structure of compacted soil by means of soil–water characteristics. The influence of inherent fabric on the mechanical properties of sand has been disclosed by many researchers, for example, Author and Menzies (1972), Oda (1972), Tatsuoka (1980), Haruyama (1981), Ochiai and Lade (1983) and Miura and Toki (1984). Informed by these findings, the effect of differences in compaction conditions on changes in mechanical properties will be discussed with a focus on the fabric of compacted soil.

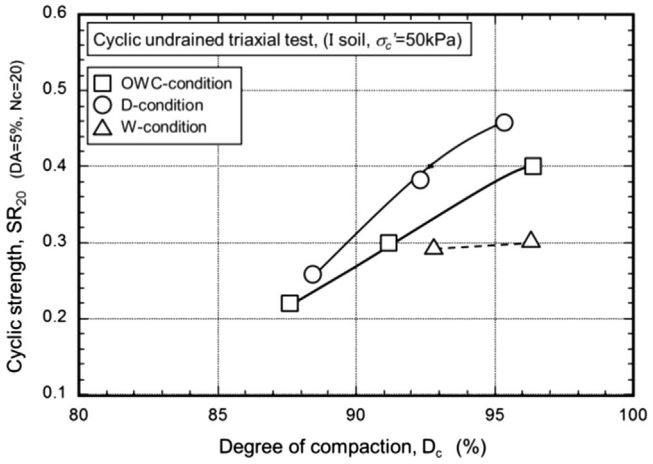

Fig. 25. Relationship between the cyclic strength SR_{20} and the degree of compaction.

Fig. 28 schematically illustrates the fabric change of compacted soil. In this discussion, it is assumed that the soil is compacted by the same energy. In this figure, large and small objects are expressed as coarse and fine particles, respectively. It is assumed that: (i) the geometry of coarse particles primarily controls the undrained compression strength and shear modulus at the small strain level, and, (ii) the geometry of fine particles controls the permeability. Based on the above assumptions, the mechanism for change in mechanical properties is discussed.

If the soil is compacted at the optimum water content, the soil becomes rigid and very dense (Fig. 28(a)). Therefore, the shear strength and shear modulus increases in value. Where conditions were drier than the optimum water content, the test results denote that the shear strength and shear modulus are less than those of the optimum water content. At the drier compaction, based on the above mentioned results, it was found that the compacted specimen has high shear strength, high permeability and slightly small shear modulus. These results may indicate that coarse-grained soil particles lay horizontally in the specimen. Generally, it is well known that the geometry of soil particles can control the shear modulus and strength. It is established that the amount of coarse particles controls the shear modulus and shear wave velocity. Hence, high shear modulus is expected from near vertical geometry of coarse particles (Sahaphol et al., 2005; Sahaphol and Miura, 2005). Additionally, the results of the permeability tests discussed above indicated that compaction under the drier condition results in high permeability in specimens. Therefore, it is hypothesized that the fine particles stand up vertically in the specimen (Fig. 28(b)). This behavior may be induced by compaction with a low degree of saturation or high suction. On the other hand, at the wetter condition, the geometry of compacted soil appears to take an inverse pattern from that of the drier condition because the shear modulus is slightly higher, and the shear strength and permeability coefficient are lower than that at the optimum water content. From this result, it is proposed that the coarse-grained particles rise up vertically while the fines particles lay horizontally (Fig. 28(c)).

Table 2
Summary of test results.

D_c (%)	q_{max}(kN/m^2)			k/k^*			G_{BE}/G^*_{BE}			SR_{20}/SR^*_{20}		
	OWC-condition	*D-condition*	*W-condition*	*OWC-condition*	*D-condition*	*W-condition*	*OWC-condition*	*D-condition*	*W-condition*	*OWC-condition*	*D-condition*	*W-condition*
85	66.5			61.3			0.46					
87.5	96.5			21.5			0.53			0.55		
90	139			11.0			0.61			0.75	0.77	
95	290	182	182	2.7	4.2	1.1	0.81	0.81	0.81		1.15	0.75
97	390			1.0			1.0			1.0		0.73

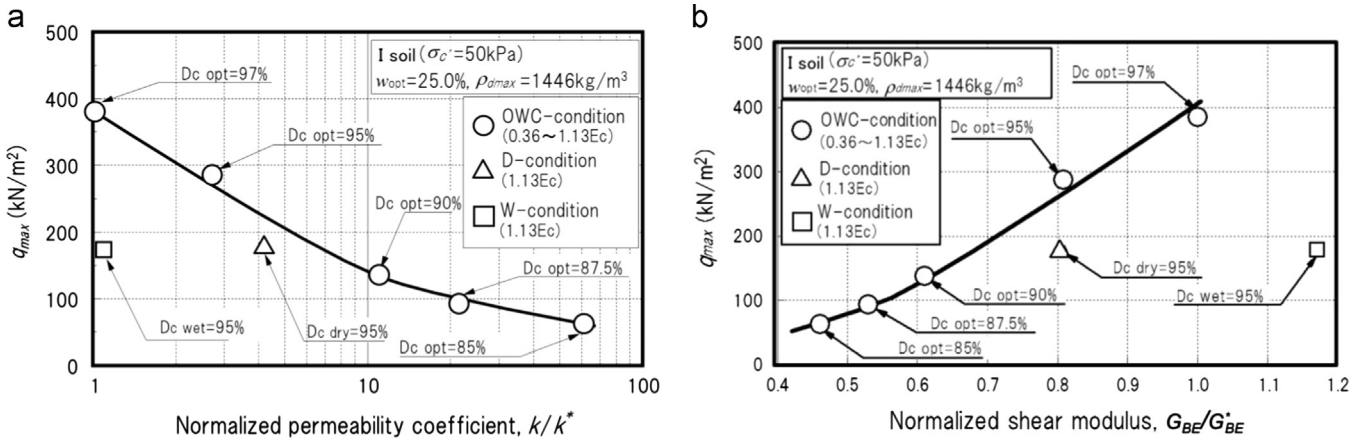

Fig. 26. Relationships between undrained strength and mechanical property; (a) undrained strength - normalized permeability coefficient relation, (b) undrained strength - normalized shear modulus relation.

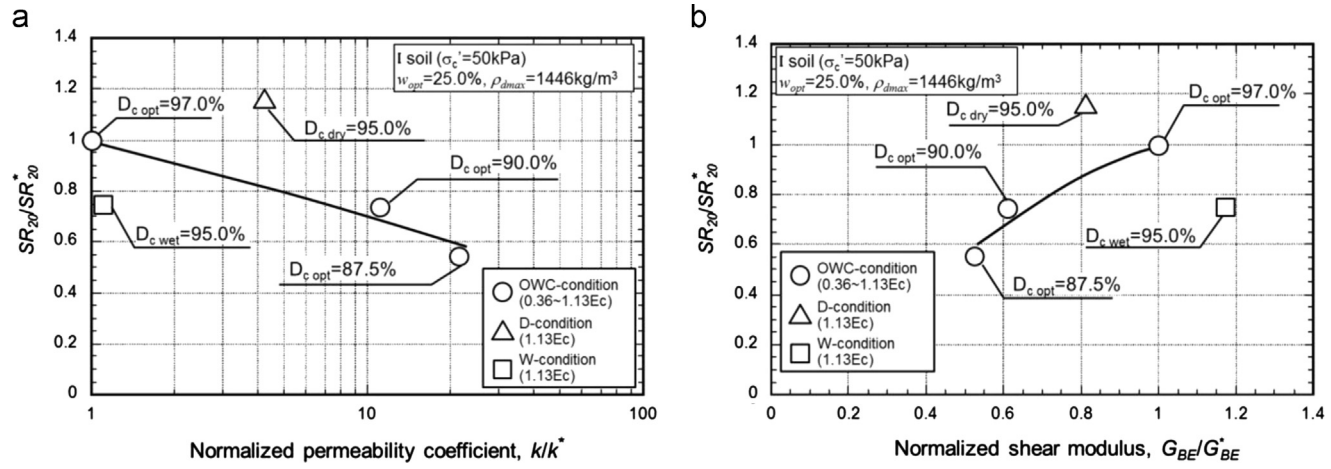

Fig. 27. Relationships between cyclic strength and mechanical property; (a) normalized cyclic strength—normalized permeability coefficient relation, (b) normalized cyclic strength—normalized shear modulus relation.

The relationship between the cyclic strength and inherent fabric of clean sand has been previously examined (for example, Ladd, 1974; Miura and Toki, 1982). These studies indicate that the cyclic strength of sand was strongly affected by its inherent fabric in terms of orientation angles of sand particles. In the present study, it has been revealed that cyclic undrained strength at drier conditions is higher than that of wetter conditions. The experimental findings indicated that the fabric of compacted soil at the drier condition, as depicted in Fig. 28(b), was exclusively resistant to cyclic loading. In order to interpret the mechanical characteristics of compacted soil accurately, the relationship between the fabric of soil and the condition of compaction should be recognized.

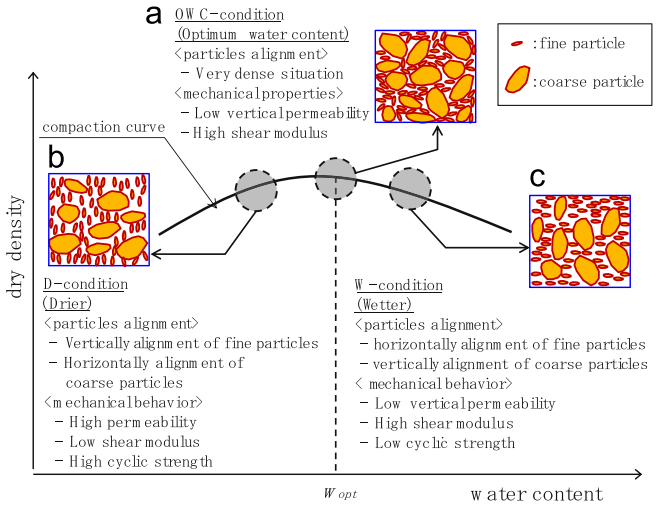

Fig. 28. A concept of fabric of compacted soil and mechanical properties; (a) OWC-condition, (b) D-condition, (c) W-condition.

6. Conclusions

On the basis of a series of laboratory tests on compacted sandy silt, the following conclusions were derived:

(1) The arrangements of soil particles were affected by the water content at compaction under the same compaction energy. Microscope observations revealed that the arrangement patterns of fine soil particles were different from that of the coarse particles.
(2) The undrained shear strength of compacted sandy silt at the optimum water content was greater than those of the other compaction conditions under the same compaction energy. The degree of compaction and water content at compaction influence the shear strength and the axial strain at failure.
(3) The relationships among shear modulus, permeability coefficient and compaction conditions were indicated. It can be confirmed that the shear modulus and the permeability coefficient were affected by the water content at compaction.
(4) Differences in water content at compaction have considerable influence on the cyclic strength characteristic despite the same degree of compaction. The specimen compacted at lower water content showed higher cyclic strength. On the other hand, it was confirmed that the undrained strength at the wetter condition was weaker than those of the other compaction cases.
(5) An increase in D_c, even an increase of over 90%, significantly improves the cyclic strength. Furthermore, this feature of the specimens at the drier than optimum water content condition become more apparent when contrasted with the wetter condition.
(6) Based on the observation results obtained by microscope, a conceptualization of the relationship between compaction conditions and the geometry of soil particles was also described. Additionally, it is suggested that there is a relationships between the anisotropy of soil and its mechanical properties under saturated condition. It was proposed that the geometry of the soil particles is related to the mechanical behavior of compacted soil.

Acknowledgement

The authors wish to express their sincere gratitude to Mr. K. Ito, Y. Hosono and R. Takada who conducted a major part of the experiment. The authors would like to thank Prof. Tatsuoka at Tokyo University of Science for his research support, and Japan's Ministry of Land, Infrastructure, Transport and Tourism for construction engineering development funding.

References

Ahmed, S., Lovell, C.W., Diamond, S., 1974. Pore sizes and strength of compacted clay. Proc. ASCE J. Geotech. Eng. Div. 100 (GT4), 407–425.
ASTM International, (2011). Standard Test Methods for Laboratory Compaction Characteristics of Soil Using Standard Effort (12,400 ft-lbf/ft^3 (600 kN-m/m^3)), Designation D698-07^{e1}, ASTM Soil Compaction Standards—A Companion CD to Manual 70 (CD-ROM).
Author, J.R. F, Menzies, B.K., 1972. Inherent anisotropy in a sand. Géotechnique 22 (1), 115–128.
Delage, P., Audiguier, M., Cui, Y., Howat, M.D., 1996. Microstructure of a compacted silt. Can. Geotech. J. 3, 150–158.
Gu, X., Yang, J., Huang, M., 2013. Laboratory measurements of small strain properties of dry sands by bender element. Soils Found. 53 (5), 735–745.
Haruyama, M., 1981. Anisotropic deformation-strength characteristics of an assembly of spherical particles under three dimensional stresses. Soils Found. 21 (4), 41–55.
Heitor, A., Indraratna, B., Rujikiatkamjorn, C., 2013. Laboratory study of small-strain behavior of a compacted silty sand. Can. Geotech. J. 50, 179–188.
Ito, K., Yokohama, S., Miura, S., Matsumura, S., 2012. Effect of compaction condition on undrained mechanical properties of embankment materials, Technical report, Hokkaido branch. Jpn. Geotech. Soc. 52, 81–88 (in Japanese).
Jafari, M.K., Shafiee, A., 2004. Mechanical behavior of compacted composite clays. Can. Geotech. J. 41, 1152–1167.
Jotisankasa, A., Coop, M., Ridley, A., 2009. The mechanical behavior of an unsaturated compacted silty clay. Géotechnique 59 (5), 415–428.
Ladd, R.S., 1974. Specimen preparation and liquefaction of sand. Proc. ASCE J. Geotech. Eng. Div. 100 (GT10), 1180–1184 (1974).
Lambe, T.W., 1958a. The structure of compacted clay. Proc. ASCE J. Soil Mech. Found. Div. 84 (SM2) (Proc. No. 1654).
Lambe, T.W., 1958b. The engineering behavior of compacted clay. Proc. ASCE J. Soil Mech. Found. Div. 84 (SM2) (Proc. No. 1655).
Lawton, E.C., Fragaszy, R.J., Hardcastle, J.H., 1991. Stress ratio effects on collapse of compacted clayey sand. J. Geotech. Eng., ASCE 117 (5), 714–730.
Mitchell, J.K., 1960. Fundamental aspects of thixotropy in soils. Proc. ASCE J. Soil Mech. Found. Div. 86 (SM3), 19–52.
Mitchell, J.K., Hooper, D.R., Campanella, R.G., 1965. Permeability of compacted clay. Proc. ASCE J. Soil Mech. Found. Div. 91 (SM4), 41–65.
Miura, S., Toki, S., 1982. A sample preparation method and its effect on static and cyclic deformation-strength properties of sand. Soils Found. 22 (1), 61–77.
Miura, S., Toki, S., 1984. Anisotropy in mechanical properties and its simulation of sand sampled from natural deposits. Soils Found. 24 (3), 69–84.
Modoni, G., Koseki, J., Anh Dan, L.Q., 2011. Cyclic stress-strain response of compacted gravel. Géotechnique 61 (6), 473–485.
Ochiai, H., Lade, P.V., 1983. Three-dimensional behavior of sand with anisotropic fabric. Proc. ASCE J. Geotech. Eng. Div. 109 (GT10), 1313–1328.

Oda, M., 1972. Initial fabrics and their relations to mechanical properties of granular material. Soils Found. 12 (1), 17–36.
Onitsuka, K., Hayashi, S., Yoshitake, S., Oishi, H., 1979. Studies of compression and strength anisotropy of compaction soils. Soils Found. 19 (3), 149–156 (in Japanese).
Runigo, B.L., Cuisinier, O., Cui, Y.J., Ferber, V., Deneele, D., 2009. Impact of initial state on the fabric and permeability of a lime-treated silt under long-term leacing. Can. Geotech. J. 46, 1243–1257.
Seed, H.B., Woodward, R.J., Lundgren, R., 1962. Prediction of swelling potential for compacted clays. Proc. ASCE J. Soil Mech. Found. Div. 88 (SM3), 53–87.
Sahaphol, T., Miura, S., Yara, K., 2005. Effect of consolidation time on shear modulus of crushable volcanic soils. Soils Found. 45 (5), 115–119.
Sahaphol, T., Miura, S., 2005. Shear moduli of volcanic soils. Soil Dyn. Earthquake Eng. 25 (2), 157–165.
Sawangsuriya, A., Edil, T.B., Bosscher, P.J., 2008. Modulus–suction–moisture relationship for compacted soils. Can. Geotech. J. 45, 973–983.
Senetakis, K., Anastasiadis, A., Pitilakis, K., 2013. Normalized shear modulus reduction and damping ratio curves of quartz sand and rhyolitic crushed rock. Soils Found. 53 (6), 879–893.
Taibi, S., Fleureau, J.M., Abou-bekr, N., Zerhouni, M.I., Benchouk, A., Lachgueur, K., Souli, H., 2011. Some aspects of the behaviour of compacted soils along wetting paths. Ge'otechnique 61 (5), 431–437.
Tatsuoka, F., 1980. Stress-strain behavior of an idealized anisotropic granular material. Soils Found. 20 (3), 75–90.
Tarantino, A., Tombolato, S., 2005. Coupling of hydraulic and mechanical behaviour in unsaturated compacted clay. Géotechnique 55 (4), 307–317.
Thu, T.M., Rahardjo, H., Leong, E., 2007. Soil-water characteristics curve and consolidation behavior for a compacted silt. Can. Geotech. J. 44, 266–275.
Vanapalli, S.K., Fredlund, D.G., Pufahl, D.E., 1999. The influence of soil structure and stress history on the soil–water characteristics of a compacted till. Géotechnique 49 (2), 143–159.
Watabe, Y., Leroueil, S., Le Bihan, J.,-P., 2000. Influence of compaction conditions on pore-size distribution and saturated hydraulic conductivity of a glacial till. Can. Geotech. J. 37, 1184–1194.
2011 Committee for Geo-hazards during Earthquakes and Mitigation Measures, 2011. Geo-hazerds During Earthquakes and Mitigation Measures—Lessons and Recommentations from the 2011 Great East Japan Earthquake. The Japanese Geotechnical Society ⟨http://www.jian.or.jp⟩.